Quasistationary Plasma Predator-Prey System of Coupled Turbulence, Drive, and Sheared E×B Flow During High Performance DIII-D Tokamak Discharges

K. Barada, T. L. Rhodes, K. H. Burrell, L. Zeng, L. Bardóczi, Xi Chen, C. M. Muscatello, and W. A. Peebles

Phys. Rev. Lett. **120**, 135002 — Published 27 March 2018

DOI: 10.1103/PhysRevLett.120.135002

A new, quasi-stationary plasma predator-prey system of coupled turbulence, drive, and sheared E×B flow during high performance DIII-D tokamak discharges

K. Barada[1], T. L. Rhodes[1], K. H. Burrell[2], L. Zeng[1], L. Bardóczi[1], Xi Chen[2], C.M. Muscatello[2], and W. A. Peebles[1]
[1]Department of Physics and Astronomy, University of California-Los Angeles, Los Angeles, CA 90095, USA
[2]General Atomics, P.O. Box 85608, San Diego, CA 92186-5608, USA

A new, long-lived limit cycle oscillation (LCO) regime has been observed in the edge of near zero torque high-performance DIII-D tokamak plasma discharges. These LCOs are localized and comprised of density turbulence, gradient drives, and E×B velocity shear damping (E and B are the local radial electric and total magnetic fields). Density turbulence sequentially acts as a predator (via turbulence transport) of profile gradients and a prey (via shear suppression) to the E×B velocity shear. Reported here for the first time, a unique spatiotemporal variation of the local E×B velocity which is found to be essential for the existence of this system. The LCO system is quasi-stationary, existing from 3 to 12 plasma energy confinement times (~30 to 900 LCO cycles) limited by hardware constraints. This plasma system appears to contribute strongly to the edge transport in these high-performance and transient-free plasmas as evident from oscillations in transport relevant edge parameters at LCO timescale.

Suppression or avoidance of edge localized modes (ELMs) during high confinement plasma operation is believed essential in magnetic fusion reactors as they have the potential to damage plasma facing components by transient heat loading[1]. Quiescent High confinement plasma operation (or QH-mode[2-4]) avoids these deleterious ELMs due to the presence of edge harmonic oscillations (EHOs), which are strong coherent magnetic fluctuations of kink-peeling type believed to be destabilized by edge rotational shear[5]. The EHO has been shown to strongly contribute to edge transport[6] that is necessary to maintain the QH-mode in a stationary ELM-free state. In this letter, observation of a new long-lived limit cycle oscillation (LCO) regime is presented that replaces the EHOs during QH-mode operation at very low applied torque from neutral beam injection (NBI). This plasma state is found to be regulated by a complex and novel predator-prey type system comprised of density turbulence ñ, profile gradients, E×B poloidal velocity ($v_{E\times B}$), and E×B velocity shear ($v'_{E\times B}$). In this regime, the edge plasma oscillates between a high $v'_{E\times B}$-low ñ and low $v'_{E\times B}$-high ñ state. In contrast to earlier reported transient plasma predator-prey systems[7-10], these oscillations are found to persist for three to twelve energy confinement times (~30-900 LCO cycles), limited only by hardware constraints. In addition, background edge densities, temperatures, gradients, plasma rotation etc., while oscillating at the LCO frequency, remain in a quasi-stationary state. The physics of these LCOs, their connection to plasma transport, and their role in a predator-prey type system all in the absence of coherent EHOs and ELM activity are the focus of this letter.

The results discussed here are obtained during recent QH-mode experiments[11] on the DIII-D tokamak (minor and major radii a ~0.67 m and R ~1.7 m). Temporal variations of important discharge parameters for the low torque QH-mode plasma discussed in this letter are shown in Fig. 1. This discharge has plasma current, I_P ~ 1 MA, on-axis magnetic field, B_T ~ 2.1 T, double null plasma shaping, plasma elongation of ~1.9, and triangularity ~0.67. NBI is used to control both injected heating power and torque. The plasma shown in Fig. 1 has been in a QH-mode state for many energy confinement times (L-H transition occurs at ~ 955 ms and QH-mode starts at ~1130 ms with the appearance of coherent EHOs). When the NBI torque is ramped down (Fig. 1a) (using oppositely directed NBI injection around 2000 ms), the discharge transitions into an improved regime with higher and wider (Fig. 1c) pedestal at ~2385 ms followed by a stronger reappearance of coherent EHOs. Here the term pedestal refers to the steep gradient region (either temperature, density, or both) generally located in the edge plasma. This operational regime is known as the wide-pedestal QH-mode[11] which remains ELM-free for many energy-confinement times ($\sim 3-12\tau_E$). When NBI torque is ramped down further (~2.5Nm to ~0 Nm), the coherent EHO eventually disappears (Fig. 1b) at ~3257 ms qualitatively consistent with theoretical predictions[5] that a critical rotational shear is required to destabilize the EHOs. This is almost immediately followed by the beginning of a different type of oscillations that will later be shown to be of limit cycle type and that are the manifestation of a complex predator-prey type system. These LCOs, with a frequency f_{LCO} ~ 55 Hz, are sustained for a period of ~ $4\tau_E$ in the discharge shown in Fig. 1 but can exist for much longer periods of up to ~$12\tau_E$. In the following we focus on the shot shown in Fig. 1 as a representative example of more than 60 similar QH-mode discharges exhibiting this behavior.

These LCOs are observed in multiple edge parameters including electron temperature from electron cyclotron emission (Fig. 2a), divertor D_α emission (Fig. 2b), edge Langmuir probe ion saturation current (Fig. 2c), and radial electric field from charge exchange recombination (CER) spectroscopy[12] (Fig. 2d). These oscillations are outside of

the respective measurement uncertainties and RMS variations (error bars and uncertainties are indicated in Fig. 2 and its caption). These oscillations are not ELMs as they have neither magnetic precursors[13] nor does the divertor D-alpha signal have a sudden rise followed by a slow decay characteristic of ELMs[13]. Oscillations due to noise in external actuators (e.g. NBI power oscillations, magnetic power supply variations, plasma current, etc.) were examined in detail and excluded as the source of these phenomena. It should be mentioned that stationary temperature oscillation regimes[14] have been reported before in the core of Tore Supra where turbulence was believed to be periodically suppressed by changes in magnetic shear induced by lower hybrid current drive. However, turbulence was not measured in that experiment.

Spatially, temporally, and wavenumber resolved density fluctuation (ñ) amplitude and its lab frame perpendicular velocity ($v_\perp$) are measured by an eight channel Doppler Backscattering (DBS) diagnostic[15] system. ñ dominantly from the cutoff layer backscatters the incident wave (probe frequency 55-75 GHz) and the 180˚ backscattered radiation is collected when the Bragg condition ($k_{\tilde{n}} = -2k_i$, where $k_{\tilde{n}}$ and k_i are the fluctuation and incident wavenumbers at the scattering location) for scattering is fulfilled. The backscattered signal is Doppler shifted with respect to the incident wave with a Doppler shifted frequency, $f_D = k_{\tilde{n}} v_\perp / 2\pi$. Here $v_\perp \sim v_{E\times B} + v_{ph}$, v_{ph} is the turbulence phase velocity, and the intensity of the received signal is proportional to ñ^2. Near the DBS cutoff location, the Doppler shifted DBS signal is dominated by poloidal wavenumbers k_θ and poloidal velocity, v_θ of ñ so that $f_D = k_\theta v_\theta / 2\pi$ [15]. The DBS data are acquired at 8 MHz sampling frequency with the RMS density fluctuation level ñ and flow velocities obtained from averages over ~320 μs which sets the time resolution. The locations of the cutoffs and fluctuation wavenumbers are estimated using the 3D ray-tracing code GENRAY[16]along with measured density profiles and reconstructed magnetic equilibrium (the latter via the EFIT[17] code). Using the measured Doppler shifted ñ frequency and the estimated wavenumber from GENRAY, the poloidal turbulence flow velocity in the laboratory frame is determined. This velocity is often dominated by the local E×B velocity in the pedestal. In this case, linear TGLF[18] simulation results[19] obtained in a similar discharge estimated a plasma frame phase velocity of these DBS observed intermediate-k fluctuations to be less than 1 km/s which is to be compared to the DBS estimated velocities of ~ 15–30 km/s discussed here. Thus, the DBS measured Doppler frequency shifts are dominated by the local $v_{E\times B}$ allowing its calculation via $2\pi f_D = k_\theta v_{E\times B}$. The measured ñ have wavenumbers in the range $0.9 \le k_\theta \rho_s \le 1.8$, typical of trapped electron modes (TEM) like instabilities where ρ_s is the ion Larmor radius using $T_e = T_i$.

Shortly after the coherent EHOs disappear at ~3257 ms, the Doppler shifted DBS ñ fluctuation spectrogram shows intermittent bursts of turbulence (Fig 2e). Both mean Doppler shifted frequency (Fig 2f) and rms ñ amplitude (Fig 2g) show oscillations with periods similar to those observed in Fig 2 (a)-(d). The shaded regions in fig 2 show a typical single cycle of the limit cycle regime. For the remaining part of this letter, the time period of rapidly increasing ñ amplitude in the beginning of the shaded region will be referred as phase 1, the rapidly decreasing ñ amplitude time period as phase 2, and the long-time duration when ñ slowly increases as phase 3 (refer Fig. 2e). There is a clear temporal correspondence between turbulence amplitude ñ, divertor D_α emission, radial electric field, and Langmuir probe ion saturation current (Fig. 2) even though these measurements are well separated toroidally and poloidally. The evolution of density profiles during one limit cycle (times marked with arrows at the top of Fig. 2) is shown in Fig. 3a. It can be clearly seen that the pedestal density gradient changes during one limit cycle and the changes are more evident towards the top of the pedestal. For the same times, a different response is observed in the electron temperature radial profiles (Fig. 3b) measured by Thomson scattering. Electron pressure profiles also show variations during one LCO period (Fig. 3c).

Figures 4 (a)-(d) show the phase space plots of local absolute $v_{E\times B}$ and ñ amplitude measured by DBS at four probed locations (for clarity only four of eight positions are shown). A clear limit cycle type oscillation is evident. Clockwise rotation is observed showing that flow first decreases when ñ increases (phase 1 in Fig 4c) and then when ñ starts to decrease, flow reaches a minimum before increasing (phase 2 in Fig 4c). Phase 3 follows in which changes in flow velocity and ñ are less compared to other phases. This observation is quite different to that reported in LCOs involving zonal flows[7-10]. These latter occur during L-H transitions where $v_{E\times B}$ increases as ñ increases to its maximum value. The current understanding is that flow alone cannot suppress ñ whereas local $v'_{E\times B}$, which depends on spatiotemporal evolution of local $v_{E\times B}$, can affect ñ amplitude[9]. To examine this, the local $v'_{E\times B}$ is calculated by interpolating the calculated absolute velocity shear between the DBS probed locations. The resulting $v'_{E\times B}$–ñ phase spaces corresponding to the respective locations in Fig 4 (a)-(d) are shown in Fig 4(e)-(h). These phase spaces also show a clear limit cycle type behavior. For clarity, Fig. 4(g) shows the same temporal phases of the cycle as shown in Fig 4(c). A counter-clockwise rotation is seen consistent with a predator–prey type relation where $v'_{E\times B}$, acting as a predator, lags the prey, ñ. For example, ñ increases in phase 1 as the shear (i.e. suppression) decreases. This then reverses in phase 2 with ñ decreasing as $v'_{E\times B}$ (suppression) increases. The reduction in $v'_{E\times B}$ in the later part of phase 2 is due to the spatiotemporal variation of $v_{E\times B}$ in the presence of very little ñ (as will be

shown later). The eventual increase of ñ in phase 3 is due to the increased gradient drive as discussed next.

The phase spaces of electron temperature gradient (∇T_e) vs ñ and $v'_{E\times B}$ vs ñ are shown in Fig. 5 for a radial location where high resolution ECE measurements are available (the same times as in Fig 4 but a different radial location). In phase 1, there is a large increase in ñ (~×3) that is due to the large decrease (~60%) in shear suppression (Fig. 5b) even with a small decrease (~10%) in gradient drive (Fig. 5a). In phase 2, ñ decreases by ~78% while ∇T_e decreases by only~20%. However, $v'_{E\times B}$ increases nearly three times indicating again its dominant role in regulating ñ. However, a large increase (~50%) in ∇T_e drive occurs in phase 3 that appears to compensate for the change in shear suppression leading to a small increase in ñ. The data in Figs. 4 and 5 indicate a unique system where the fluctuations sequentially act as both a predator (on the gradient drive and resulting $v_{E\times B}$) and a prey (of the velocity shear suppression). In the above, although the phase space of ∇T_e and ñ is described, inclusion of ∇n_e does not change the physical picture. Overall, the data appear consistent with the picture of an interrelated system of ñ, ñ driven transport, ∇T_e drive, and velocity shear.

The spatiotemporal evolution of ñ, $v_{E\times B}$, and $v'_{E\times B}$ at four DBS locations and for three LCO periods are shown in Fig 6. The phases 1-3 (in Fig. 4c, 4g and Fig. 5) are indicated by the horizontal arrows above Fig 6a. ñ (Fig. 6a) starts to grow nearly at the same time for all locations (during phase 1) but peaks with a time delay in inner probed locations. In phase 1, when $v_{E\times B}$ is decreasing, radial variations in the decrease of $v_{E\times B}$ results in a decreased velocity shear $v'_{E\times B}$ (see fig 6c). Later, the temporal delay in the increase of $v_{E\times B}$ in inner locations during phase 2 leads to increase in $v'_{E\times B}$. In the later part of phase 2, when ∇T_e and $v_{E\times B}$ start to increase after ñ is suppressed, $v'_{E\times B}$ starts to decrease. The existence and evolution of the time varying velocity shear (e.g. Fig 6c) is made possible due to the delay in the evolution of $v_{E\times B}$ from mid-pedestal towards the top of pedestal (e.g. Fig. 6b). It is this 2D evolution (time and space) that provides the physical understanding of how this system arises. Changes in the far edge do not immediately appear further inward. There is a wavelike propagation of these perturbations due to this which is very similar to the core LCO observed in reference 14. Sustained predator-prey oscillations in a Lotka-Volterra system have been previously examined[20,21] showing that when diffusion is added, the LCO system can achieve a stationary state in the presence of random population noise. This radially inward propagation might mimic the diffusion and possibly be the reason behind the sustained oscillations reported here and also in the reported core oscillations[14,21]. Diffusion is expected to be nonlinear in tokamak plasmas and should inspire modeling efforts to simulate the experimental results of stationary LCOs similar to that reported in reference 20.

Cross-correlation of $v_{E\times B}$ measured by two DBS systems probing the same plasma radius and wavenumbers but separated toroidally by 180˚ (~700 cm and poloidally by ~8.5 cm) finds a normalized cross-correlation peak C_{xy}~0.75 at time lag ~0 ms during the LCO phase. This is to be compared to a value of C_{xy}~0.1 when finite mode number ($m, n \neq 0$) EHOs are present prior to the LCO phase. This is consistent with a toroidal and poloidal symmetric nature of $v_{E\times B}$ during the LCO regime. However, the clockwise phase behavior in Fig 4(a)-(d) indicate that while ñ increases to its maximum, $v_{E\times B}$ is decreasing in contrast to the transient LCOs reported in references [7-10].

The discharge discussed so far encounters an ELM coincident with LCO cessation at ~3944 ms for reasons not completely understood at this time. In a similar plasma (shot# 164884) but with lower chord averaged density and pedestal pressure, the LCO phase is sustained for $12\tau_e$ (f_{LCO}~500 Hz) without encountering an ELM.

The observations thus indicate a likely link between the LCO, turbulence, and turbulence induced transport. Indeed, the Langmuir probe ion saturation current (proportional to local ion particle flux) (Fig. 2c) is consistent with transport events modulated at f_{LCO}. A survey of all existing wide-pedestal QH-mode discharges (>60) finds that the LCOs described here are always present when the EHO is absent. The LCO frequency is found to scale inversely with the pedestal density while the LCO edge T_e perturbation amplitude decreases with f_{LCO}. This will be a focus of future work. Power balance calculations of thermal transport indicate no significant changes in going from EHO to LCO dominated plasmas. This is consistent with the LCO, possibly in combination with broadband magnetic fluctuations[11], replacing the EHO dominated edge transport. LCO regulation of transport in the wide-pedestal may therefore play an important role in sustaining the pedestal pressure below the ELM trigger limit and could lead to a low torque, transient-free operation (i.e. ELM-free) of large tokamaks such as ITER[22]. The observations and physics understanding presented here will present useful challenges to gyrokinetic simulations[23] and analytic treatments such as Lotka-Volterra type modelling[24].

Acknowledgements

This work was supported in part by the U.S. Department of Energy under DE-FC02-04ER54698 and DE-FG02-08ER54984. We want to thank Prof P. H. Diamond and Dr. L. Schmitz for useful and detailed physics discussion.

References

[1] T. E. Evans, Journal of Nuclear Materials 438, S11 (2013).
[2] K. H. Burrell *et al.*, Phys. Plasmas 12, 056121 (2005).
[3] W. Suttrop *et al.*, Nucl. Fusion 45, 721 (2005).
[4] Y. Sakamoto *et al*., Plasma Phys. Control. Fusion 46, A299 (2004).
[5] P. B. Snyder *et al.*, Nucl. Fusion 47, 961 (2007).
[6] B. A. Grierson *et al.*, Phys. Plasmas 22, 055901 (2015).
[7] L. Schmitz, L. Zeng, T. L. Rhodes, J. C. Hillesheim, E. J. Doyle, R. J. Groebner, W. A. Peebles, K. H. Burrell, and G. Wang, Phys. Rev. Lett. 108, 155002 (2012).
[8] J. Cheng *et al*, Nucl. Fusion Phys. 54, 114004 (2014).
[9] T. Estrada et al., Europhys. Lett. 92, 35001 (2010).
[10] G. S. Xu *et al.*, Phys. Rev. Lett. 107, 125001 (2011).
[11] K. H. Burrell *et al*., Phys. of Plasmas 23, 056103 (2016).
[12] P. Gohil, K. H. Burrell, and T. N. Carlstrom, Nucl. Fusion 38, 93, (1998).
[13] H. Zohm, Plasma Phys. Control. Fusion 38, 105 (1996).
[14] G. Giruzzi *et al*., Phys. Rev. Lett. 91, 135001 (2003).
[15] W.A. Peebles *et al*., Rev. Sci. Instrum. 81, 10D902 (2010).
[16] A. P. Smirnov *et al.*, in Proceedings of the 15th Workshop on ECE and ECRH (World Scientific, Singapore, 2009), p. 301, also see www.compxco.com/genray.html.
[17] L.L. Lao, H.S. John, R.D. Stambaugh, A.G. Kellman, and W Pfeiffer. Nucl. Fusion 25,1611 (1985).
[18] G.M. Staebler G.M., J.E. Kinsey J.E. and R.E. Waltz, Phys. Plasmas 14, 055909 (2007).
[19] Xi Chen *et al*., Nucl. Fusion 57,022007 (2017)
[20] R. Abta, M. Schiffer, and N. M. Shnerb, Phys. Rev. Lett. 98, 098104 (2007).
[21] F. Turco *et al*, Phys. of Plasmas 16, 062301 (2009).
[22] ITER Physics Basis Editors *et al*., Nucl. Fusion 39, 2137 (1999).
[23] J. A. Krommes, Annual Review of Fluid Mechanics 44,175 (2012).
[24] K. Miki *et al*., Physics of Plasmas 19, 092306 (2012).

Figure Captions

Fig. 1. (a) NBI power and torque, (b) n=1 EHO amplitude as measured by Mirnov coils and chord averaged electron density, (c) Electron pedestal pressure width and electron pedestal pressure. Also, shown are the times of wide pedestal transition (solid line ~2385 ms) and EHO to LCO regime transition (dashed line ~3257ms).

Fig. 2. (a) Te at ρ~0.82 and ρ~0.91 with maximum error of 5% (b) Lower divertor Dα visible light emission intensity, (c) Ion saturation current density (maximum error~3%) from edge Langmuir probe (d) Radial electric field, (e) ñ frequency spectrum (DBS, ρ~0.91), (f) mean Doppler shifted frequency from DBS spectrum in (e), and (g) RMS ñ from integrating Doppler shifted spectrum in (e).

Fig. 3. Radial profiles of (a) electron density and (b) electron temperature, and (c) calculated electron pressure (3325 ms: solid black curve, 3333 ms: dashed blue curve, and 3339 ms: solid red curve (these times shown as arrows on top of Fig 2) during an LCO cycle. Radial locations of DBS at 60º toroidal angle (open circles) and 240º toroidal angle (open square) are shown in Fig 2a.

Figure 4 (a) –(d) Phase space plot of local $v_{E\times B}$ and ñ rms values at four DBS locations and (e)-(h) Phase space plots of local absolute $v'_{E\times B}$ and ñ rms values for respective locations shown in Figure 4 (a)-(d).

Figure 5. Phase space plots at ρ~0.91 of (a) $\nabla T_e$and ñ rms values (b) absolute $v'_{E\times B}$ and ñ rms values.

Figure 6. Temporal evolution in 3 LCO cycles of (a) ñ rms values (for clarity the ñ rms values have been normalized using the factors indicated to the right within the panel) measured at four radial locations by DBS (b) $v_{E\times B}$ measured at the same four radial locations as in (a) by DBS, and (c) $v'_{E\times B}$ calculated at ρ~0.88.

Figures with Figure captions:

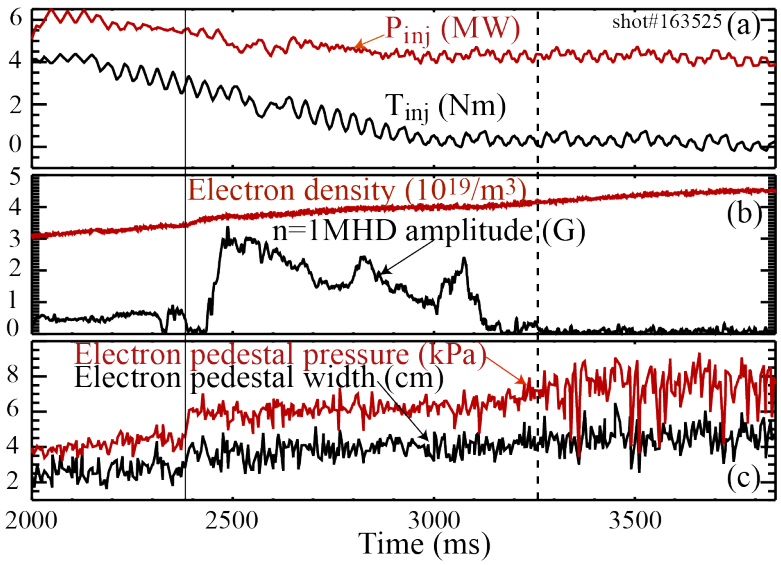

Fig. 1. (a) NBI power and torque, (b) n=1 EHO amplitude as measured by Mirnov coils and chord averaged electron density, (c) Electron pedestal pressure width and electron pedestal pressure. Also, shown are the times of wide pedestal transition (solid line ~2385 ms) and EHO to LCO regime transition (dashed line ~3257ms).

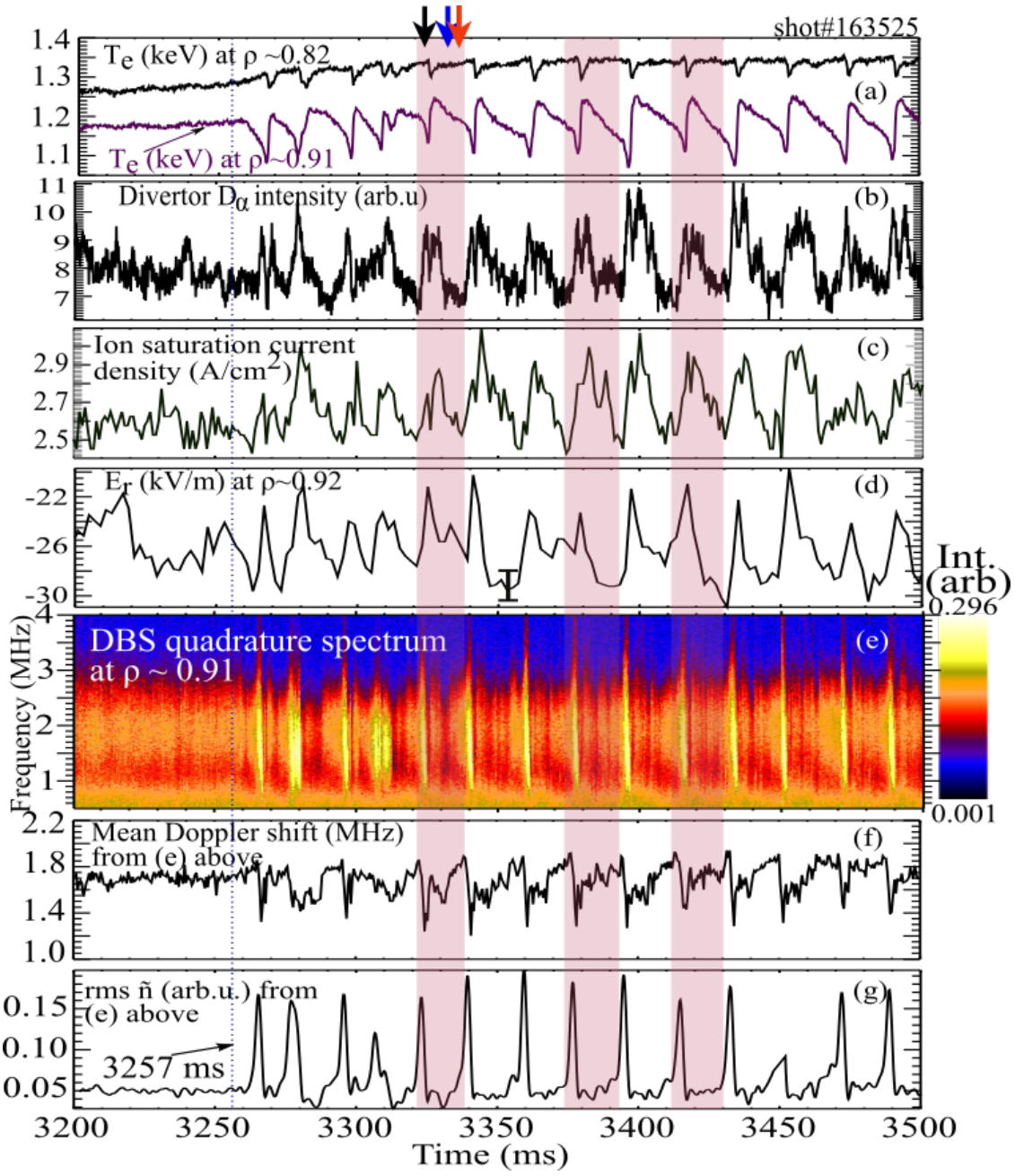

Fig. 2. (a) Te at ρ~0.82 and ρ~0.91 with maximum error of 5% (b) Lower divertor Dα visible light emission intensity, (c) Ion saturation current density (maximum error~3%) from edge Langmuir probe (d) Radial electric field, (e) ñ frequency spectrum (DBS, ρ~0.91), (f) mean Doppler shifted frequency from DBS spectrum in (e), and (g) RMS ñ from integrating Doppler shifted spectrum in (e).

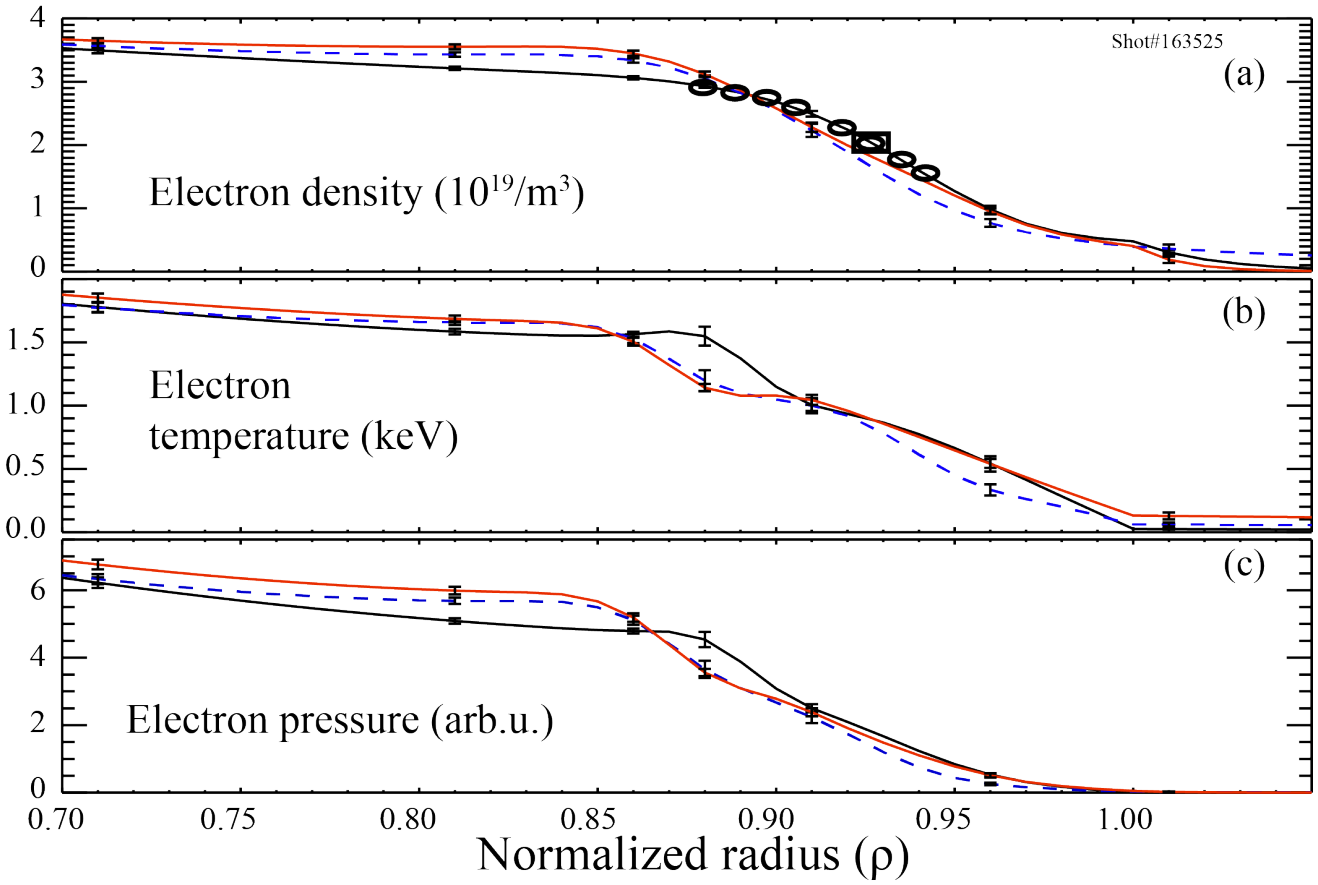

Fig. 3. Radial profiles of (a) electron density and (b) electron temperature, and (c) calculated electron pressure (3325 ms: solid black curve, 3333 ms: dashed blue curve, and 3339 ms: solid red curve (these times shown as arrows on top of Fig 2) during an LCO cycle. Radial locations of DBS at 60º toroidal angle (open circles) and 240º toroidal angle (open square) are shown in Fig 2a.

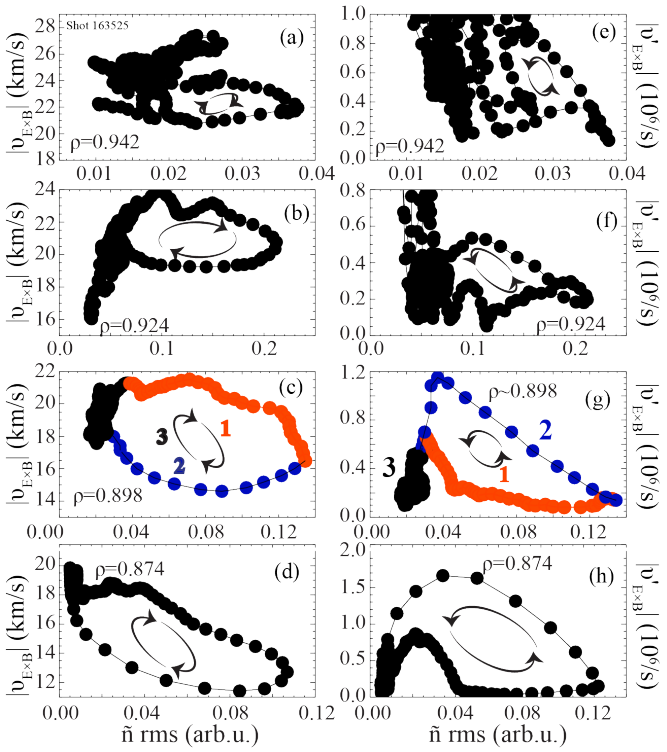

Figure 4 (a) –(d) Phase space plot of local $\upsilon_{E\times B}$ and ñ rms values at four DBS locations and (e)-(h) Phase space plots of local absolute $\upsilon'_{E\times B}$ and ñ rms values for respective locations shown in Figure 4 (a)-(d).

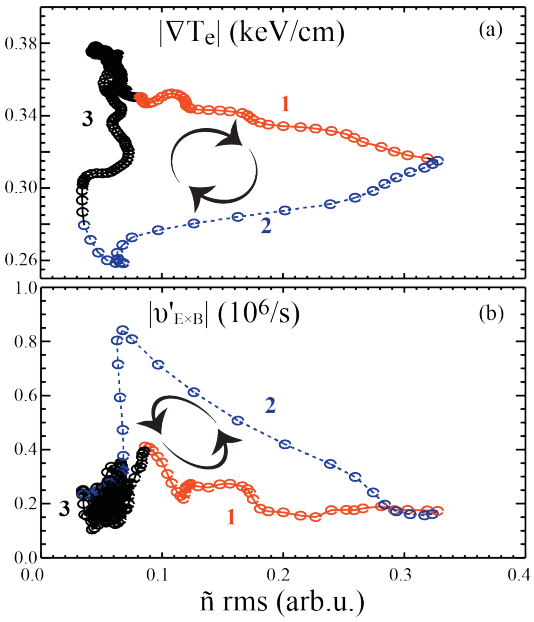

Figure 5. Phase space plots at ρ~0.91 of (a) $\nabla T_e$and ñ rms values (b) absolute $\upsilon'_{E\times B}$ and ñ rms values.

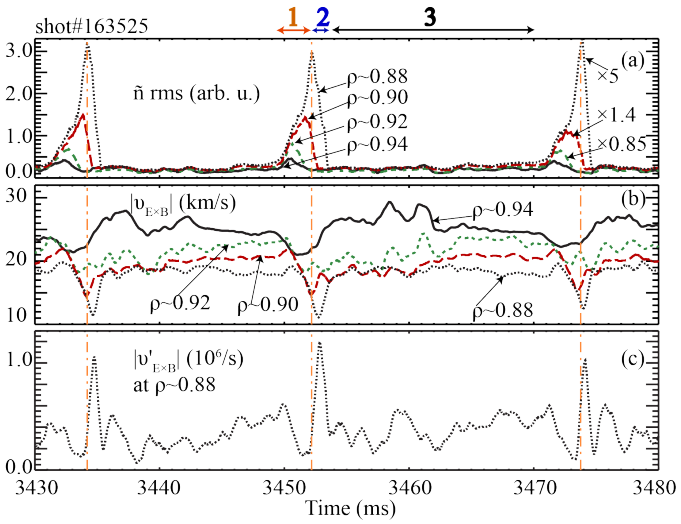

Figure 6. Temporal evolution in 3 LCO cycles of (a) ñ rms values (for clarity the ñ rms values have been normalized using the factors indicated to the right within the panel) measured at four radial locations by DBS (b) $\upsilon_{E\times B}$ measured at the same four radial locations as in (a) by DBS, and (c) $\upsilon'_{E\times B}$ calculated at ρ~0.88.